Editors' Suggestion

Effect of a forward-facing step on the disturbance amplification in a flat-plate boundary layer

Nathaniel Hildebrand,[1,*] Pedro Paredes,[2] and Meelan M. Choudhari[1]
[1]*Computational AeroSciences Branch, NASA Langley Research Center, Hampton, Virginia 23681, USA*
[2]*National Institute of Aerospace, Hampton, Virginia 23666, USA*

(Received 10 October 2024; accepted 25 March 2025; published 14 April 2025)

We apply linear stability analysis to nearly incompressible flow over a two-dimensional zero-pressure-gradient boundary layer in the presence of a forward-facing step (FFS), with step height to local displacement thickness ratios between $0 < h/\delta_s^* < 3.2$. We employ a nominally sharp FFS with a 1 μm radius to closely resemble a prior wind tunnel experiment, but we also examine the impact of various step corner radii and slopes. The Navier-Stokes equations are solved on curvilinear grids to obtain the laminar basic states. After that, we use a combination of the harmonic linearized Navier-Stokes equations and the parabolized stability equations to compute the linear amplification of Tollmien-Schlichting instabilities. The N-factor envelopes for the FFS reveal crucial differences with respect to those obtained previously for backward-facing steps (BFS) with $0 < h/\delta_s^* < 1.3$, for which accurate predictions of transition onset could be obtained via N-factor correlations. As the boundary-layer flow recovers to its unperturbed state in the far wake of the BFS, the slope of the N-factor envelope is nearly the same as that of the unperturbed flat-plate boundary layer. In contrast, the N-factor envelope downstream of the FFS becomes flatter as the step height increases, i.e., dN/dx becomes nearly 0, which causes the N-factor method to become sensitive to the prescribed value of the correlating N-factor value. In spite of this difficulty, the N-factor method still captures the overall trend associated with a progressively upstream shift in the transition location as the FFS height becomes larger. However, the critical step height corresponding to the onset of a significant upstream shift in transition location is not very well predicted when compared with the measured data. Within the framework of a variable N-factor method, the predicted reduction in the transition N-factor is given by $\Delta N = 1.89\arctan[(h/\delta_s^* - 1.29)/0.179] - 2.73$.

DOI: 10.1103/PhysRevFluids.10.043901

I. INTRODUCTION

Significantly decreasing the fuel burn rate of new aircraft has been a major focus both in the U.S. [1] and in Europe [2] to reduce the environmental impact of aviation. One promising way to achieve this involves expanding the laminar regions on aerodynamic surfaces by preventing or delaying the onset of transition to turbulence in the boundary-layer flow, which reduces the overall skin-friction drag and increases energy efficiency. This method is referred to as laminar flow control (LFC) in the literature [3]. Various forms of LFC include natural laminar flow that utilizes airfoil design with a tailored surface pressure distribution, LFC based on some active form of flow control via surface suction and/or surface heat transfer, and hybrid LFC that combines the two methods. Spanwise arrays of discrete roughness elements have also been employed in recent years to demonstrate transition delay in a limited range of flow conditions [4]. The challenges of successfully

*Contact author: nathaniel.j.hildebrand@nasa.gov

implementing LFC include uncertainty in transition modeling, operational factors, e.g., ice accretion and insect contamination, integration of LFC with the vehicle design, and manufacturing defects, such as two-dimensional steps, gaps, surface waviness, and three-dimensional surface roughness. Our focus in this work is to perform a computational study to enable a better understanding and quantification of the effects of two-dimensional forward-facing steps (FFS), which are known to be an important contributor to an earlier onset of transition [5,6].

Accurately modeling boundary-layer transition across different speed regimes is a top research priority in the NASA CFD Vision 2030 Study [7]. Manufacturing defects and unavoidable surface roughness compound the difficulties of transition modeling by modifying the transition mechanisms in a way that leads to significantly earlier onset of transition relative to a smooth aerodynamic surface. Several different mechanisms may contribute to the effects of surface imperfections on the transition process. These include a global instability within the separation zone [8,9], convective instability waves [10], boundary-layer receptivity to freestream unsteadiness [11,12], streak instabilities within the wake region [13], or some combination of these phenomena [14]. For two-dimensional boundary layers, Tollmien-Schlichting (TS) instability waves are the most common transition mechanism, and the amplification characteristics of these instabilities can be greatly influenced by the presence of two-dimensional step excrescences, such as the FFS and the backward-facing step (BFS). Historically, the effects of FFS and BFS have been predicted with empirical criteria based on available measurements [15]. Experimental results on transition to turbulence in the presence of steps have been reported in Refs. [5,6,16–18], whereas computational studies have been reported by Refs. [6,19–22]. The effects of step excrescences on swept-wing boundary layers have also been studied in recent years; see, for instance, Refs. [23–26].

The most common approach to computationally predict transition locations for surface roughness is by using the N-factor of the most amplified unstable disturbance. Crouch *et al.* [6,27] correlated the associated jump in the N-factor envelope of TS instability waves as a linear function of the step height with experimental measurements. The change in N-factor due to a FFS is $1.6h/\delta_s^*$, and the change in N-factor due to a BFS is $4.4h/\delta_s^*$, where h and δ_s^* are the step height and boundary-layer displacement thickness, respectively [6]. Perraud and Seraudie [20] showed that for a BFS, the N-factor increases substantially just downstream of the step and then levels out becoming relatively parallel to the no-step envelope, resulting in progressive shifts of the different transition locations. However, for a FFS they showed the locations of transition onset shift abruptly. Costantini *et al.* [28] found that changes of the streamwise pressure gradient did not alter the empirical correlations for predicting FFS transition locations. Crouch and Kosorygin [29] showed that subsonic flow past a BFS with an airfoil-type pressure distribution can be represented by a variable N-factor method, but a FFS has to be positioned between the neutral point and the transition location for this method to be accurate.

A variety of other computational methods have been used to predict roughness-induced boundary-layer transition in the literature. Subsonic flow over steps and bumps have been modeled with the interactive boundary-layer equations and quasiparallel stability theory by Refs. [19,30,31]. Edelmann and Rist [21] applied direct numerical simulations (DNS) to flow over a FFS. They described the presence of two separation bubbles (i.e., one in front of the FFS, and the other directly on top of it) and the enhanced amplification of disturbances. DNS is also employed by Wise *et al.* [32] for boundary-layer flows over surface imperfections to study the effects of step height, freestream turbulence intensity, and favorable pressure gradients. Rizzetta and Visbal [33] used DNS and implicit large eddy simulation to model nonlinear disturbance evolution downstream of BFS and FFS. Dong and Zhang [34] implemented a local scattering approach with triple-deck theory to simulate low-speed flow over BFS and FFS. Thomas *et al.* [35] and Franco *et al.* [36] applied the harmonic linearized Navier-Stokes equations (HLNSE) to surface deformations.

We previously investigated low-speed boundary-layer transition over smooth BFS using linear stability theory, the parabolized stability equations (PSE), and HLNSE [22,37]. The predicted transition locations correlated well with $N_{\mathrm{tr}} = 7.6$ and showed good agreement with experimental measurements by Wang and Gaster [5] for $h/\delta_s^* < 1.3$. Within the framework of a variable

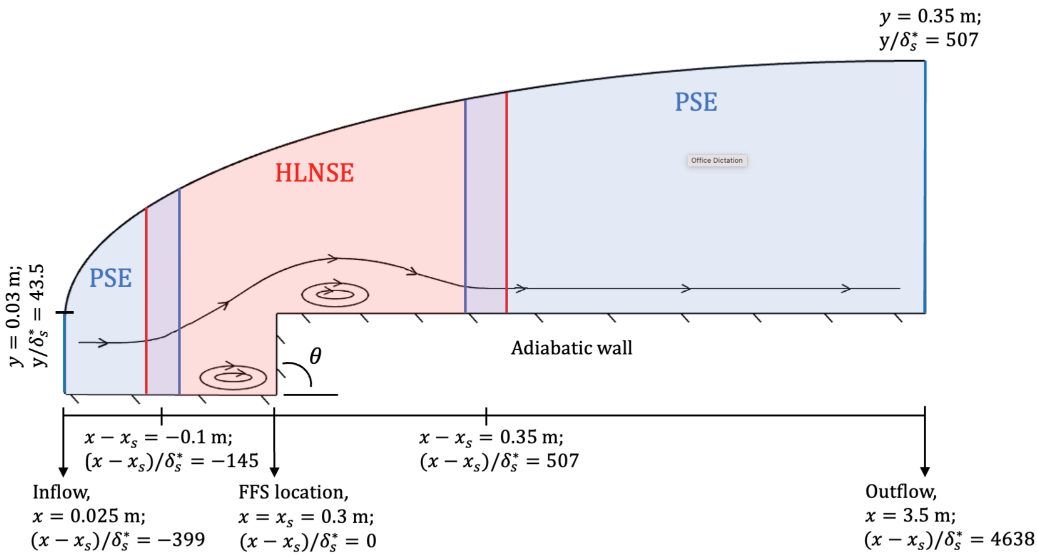

FIG. 1. Schematic of subsonic flow over a FFS with two separation bubbles. Here, $\delta_s^* = 6.9 \times 10^{-4}$ m that corresponds to $U_\infty = 28$ m/s.

N-factor method, the reduction in transition N-factor is given by $\Delta N = 2.47(h/\delta_s^*)^2 + 0.62(h/\delta_s^*)$ for $h/\delta_s^* < 0.38$ and $\Delta N = 3.0(h/\delta_s^*) - 0.55$ for $0.38 < h/\delta_s^* < 1.3$. This correlation is accurate because the net destabilization from the BFS is the dominant contributor to the resulting shift in the transition location.

The work presented here is an extension of Hildebrand *et al.* [22,37] applied to FFS instead of BFS. We use a combination of PSE and HLNSE to compute growth rates and N-factors of TS waves for the experimental configuration from Wang and Gaster [5]. Also, we explore the effect that smoothness and rounded corners of the FFS have on the N-factors and transition predictions. Section II describes the overall flow configuration and the FFS geometry. We provide details about the different numerical methods in Sec. III. The results of a zero-pressure-gradient boundary layer over a FFS are presented in Sec. IV. Finally, we provide a summary of the results and concluding remarks in Sec. V.

II. FLOW CONFIGURATION

Schematic of a low Mach number, subsonic flow over a FFS is depicted in Fig. 1. The flow configuration is based on experiments performed by Wang and Gaster [5] in the low-turbulence wind tunnel of the Engineering Department at the Queen Mary University of London. In this experiment, a flat-plate model is used with a nominally sharp FFS located at $x_s = 0.3$ m from the plate leading edge. Our computational domain extends from $x = 0.025$ m or $x - x_s = -0.275$ m to $x = 3.5$ m or $x - x_s = 3.2$ m. The domain height increases as the boundary-layer thickness grows downstream from $y = 0.03$ to $y = 0.35$ m. For these simulations, a Blasius boundary layer enters at the inlet, after which it flows downstream and undergoes flow separation in the vicinity of the FFS before reattaching behind the FFS and subsequently exiting at the outlet. The separated flow involves two distinct pockets of flow recirculation, one upstream of the FFS and the other downstream of the FFS. A no-slip adiabatic wall resides along the bottom boundary.

For the basic state computations, we employ a nonuniform grid with 6001 and 301 points in the streamwise and wall-normal directions, respectively. The first grid point above the wall is positioned so the nondimensional viscous wall spacing $y^+ = (u_\tau y)/\nu$ is equal to 0.1, where $u_\tau y$ is the friction

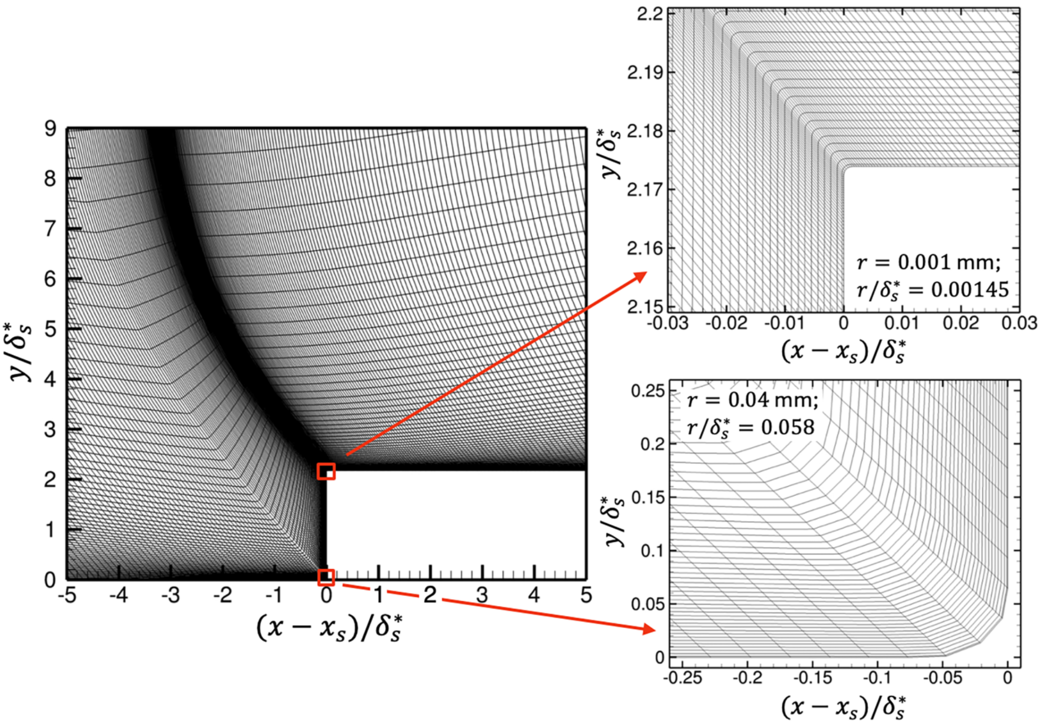

FIG. 2. Computational grid for the simulations of subsonic flow over a FFS. Closeup views of the grid near the step corners are depicted on the right. Here, $U_\infty = 28$ m/s, $\delta_s^* = 6.9 \times 10^{-4}$ m, and $h = 1.5$ mm or $\mathrm{Re}_s = 5.58 \times 10^5$ and $h/\delta^* = 2.174$.

velocity and ν is the kinematic viscosity. Figure 2 displays the basic state computational grid near the FFS. In Fig. 2, the grid spacing in the wall-normal direction is the smallest near the no-slip adiabatic wall and gradually increases from there toward the upper domain boundary. The grid spacing in the streamwise direction is the smallest near the upper corner of the FFS and gradually increases toward both the inflow and outflow boundaries. In the experiments performed by Wang and Gaster [5], the FFS is nominally sharp; however, to simplify the computational process, we apply slight rounding of the step corners. The bottom FFS corner has a radius of 4×10^{-5} m, while the top corner has a radius of 10^{-6} m. Any further reduction in the bottom corner radius does not have a significant effect on the pressure distribution or the N-factor values. As we will see later, changes to the top corner radius do impact the flow field and the N-factor values considerably. The same computational nonuniform grids used for the basic state computations are employed for the PSE and HLNSE. In Sec. IV B, we demonstrate grid convergence for both the basic state and the stability analysis results.

We selected the flow conditions to match the Wang and Gaster [5] experiments and our previous computational studies [22,37]. The freestream velocity, U_∞, varies with intervals of 2 m/s from 16 m/s to 34 m/s, the freestream temperature, $T_\infty = 292.7$ K, and density, $\rho_\infty = 1.206$ kg/m^3, are held constant. Table I lists all of the freestream velocities considered in this work, along with the freestream unit Reynolds numbers (Re_∞), the boundary-layer thicknesses (δ_s), the Reynolds numbers based on the boundary-layer thicknesses (Re_{δ_s}), the boundary-layer displacement thicknesses (δ_s^*), the Reynolds numbers based on the boundary-layer displacement thicknesses ($\mathrm{Re}_{\delta_s^*}$), and the Reynolds numbers based on the step location (Re_s). Here, $\mathrm{Re}_\infty = U_\infty/\nu_\infty$, $\mathrm{Re}_{\delta_s} = (U_\infty/\nu_\infty)\delta_s$, $\mathrm{Re}_{\delta_s^*} = (U_\infty/\nu_\infty)\delta_s^*$, and $\mathrm{Re}_s = (U_\infty/\nu_\infty)x_s$. Note the subscript "$s$" refers to the step location. The constant ratio of specific heats is $\gamma = 1.4$. Furthermore, the specific gas constant for air is

TABLE I. Freestream velocities, boundary-layer thicknesses, and Reynolds numbers corresponding to subsonic flow over a FFS. The length scales δ_s, δ_s^*, and x_s are computed or defined at the step location, while the velocity and kinematic viscosity are computed in the freestream.

U_∞ (m/s)	16	18	20	22	24	26	28	30	32	34
Re_∞ ($\times 10^6$ m^{-1})	1.07	1.20	1.33	1.46	1.60	1.73	1.86	2.00	2.13	2.26
δ_s ($\times 10^{-3}$ m)	2.65	2.50	2.37	2.27	2.17	2.08	2.01	1.94	1.88	1.82
δ_s^* ($\times 10^{-4}$ m)	9.13	8.61	8.17	7.79	7.46	7.16	6.90	6.67	6.46	6.26
Re_{δ_s} ($\times 10^3$)	2.84	3.00	3.15	3.31	3.47	3.60	3.74	3.88	4.00	4.11
$\mathrm{Re}_{\delta_s^*}$ ($\times 10^3$)	0.97	1.03	1.09	1.14	1.19	1.24	1.29	1.33	1.38	1.42
Re_s ($\times 10^5$)	3.21	3.60	3.99	4.38	4.80	5.19	5.58	6.00	6.39	6.78

$R = 287.15$ J/(K kg), and the Prandtl number is $\mathrm{Pr} = 0.72$. We use Sutherland's law to compute the dynamic viscosity, $\mu = c_1 T^{1.5}/(T + T_s)$ with $c_1 = 1.458 \times 10^{-6}$ kg/(ms $\sqrt{\mathrm{K}}$) and $T_s = 110.4$ K. Figure 3 displays the variation in both the boundary-layer thickness and the boundary-layer displacement thickness as well as the Reynolds numbers based on those values with increasing Reynolds number based on the step location. In Fig. 3, as the Reynolds number based on the step location increases, the boundary-layer thicknesses decrease and the Reynolds numbers based on the boundary-layer thicknesses increase.

III. NUMERICAL METHODOLOGY

Similar to our previous studies on BFS [22,37], the laminar basic states are computed with the fully compressible Navier-Stokes equations in a curvilinear body-fitted coordinate system. A sixth-order finite-difference scheme in both spatial directions is employed for the discretization. We use the computational nonuniform grids with $N_x = 6001$, $N_y = 301$, and $y^+ = 0.1$ described in Sec. II. The boundary conditions are the enforcement of a Blasius self-similar boundary-layer profile at the inlet, extrapolation at the outlet, a no-slip adiabatic bottom wall, and freestream along the upper boundary. We solve the resulting nonlinear system with the Newton-Raphson method that converges the residual to machine zero. MUMPS [38] is utilized to invert the large sparse matrices.

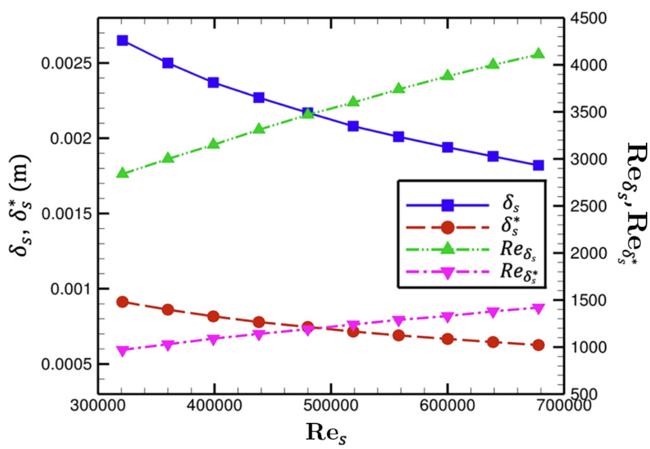

FIG. 3. Variation of the boundary-layer thicknesses and Reynolds numbers based on those values with increasing Reynolds number based on the step location. The length scales δ_s, δ_s^*, and x_s are computed or defined at the step location, while the velocity and kinematic viscosity are computed in the freestream.

Again, similar to our earlier BFS work [22,37], a combination of PSE and HLNSE is utilized to model the linear disturbance amplification over the FFS configurations of interest. HLNSE has been applied to several boundary-layer stability problems [35,36,39–41] and shown to be accurate, efficient, and robust in these cases. For the current FFS work, PSE is employed in attached flow regions with weaker streamwise variation, from $x - x_s = -0.275$ m to $x - x_s = -0.075$ m upstream of the step and $x - x_s = 0.325$ m to $x - x_s = 3.2$ m downstream of the step. Note that PSE requires the basic state and the amplitude function variables to vary slowly in the streamwise direction [42]. However, the streamwise length scale of the basic state is comparable to a representative wavelength of the instability waves in the FFS vicinity. HLNSE is used in regions of rapid mean-flow variation, including the pockets of recirculating flow near the step from $x - x_s = -0.125$ m to $x - x_s = 0.375$ m. Figure 1 displays these zones, where the blue color indicates PSE, the red color denotes HLNSE, and the purple shade corresponds to regions of overlap between PSE and HLNSE. We confirmed that the results are insensitive to variations in the sizes of these regions as long as HLNSE is used in a sufficient region surrounding the FFS to capture the correct physics due to recirculating flow and strong gradients.

The linear perturbations around the laminar basic states are harmonic in time. These perturbations are defined by the following mathematical expression:

$$\tilde{q}(x, y, z, t) = \breve{q}(x, y) \exp{[i(\beta z - \omega t)]} + \text{c.c.}, \tag{1}$$

where ω is the angular frequency and β is the spanwise wave number. Here, $\tilde{q}(x, y, z, t) = (\tilde{\rho}, \tilde{u}, \tilde{v}, \tilde{w}, \tilde{T})^{\mathrm{T}}$ is the vector of unsteady perturbation quantities, $\breve{q}(x, y) = (\breve{\rho}, \breve{u}, \breve{v}, \breve{w}, \breve{T})^{\mathrm{T}}$ is the vector of disturbance mode shapes, and $\bar{q}(x, y) = (\bar{\rho}, \bar{u}, \bar{v}, \bar{w}, \bar{T})^{\mathrm{T}}$ is the vector of basic state quantities. The disturbance mode shapes can be separated into real and imaginary components such that $\breve{q}(x, y) = \breve{q}_r(x, y) + i\breve{q}_i(x, y)$. Also, the magnitude is defined as the following $||\breve{q}|| = (\breve{q}_r^2 + \breve{q}_i^2)^{1/2}$. For the streamwise velocity component of the mode shape, $\breve{u}(x, y) = \breve{u}_r(x, y) + i\breve{u}_i(x, y)$ and $||\breve{u}|| = (\breve{u}_r^2 + \breve{u}_i^2)^{1/2}$. The disturbance functions $\breve{q}(x, y)$ satisfy the HLNSE [40] that involve coefficient functions that depend on the basic state variables/parameters and the angular frequency ω such that

$$L_{\text{HLNSE}}\breve{q}(x, y) = \breve{f}, \tag{2}$$

where $\breve{f}$ represents a potential forcing term. PSE solves an approximate form of HLNSE based on isolating rapid phase variations in the streamwise direction via the disturbance ansatz

$$\breve{q}(x, y) = \hat{q}(x, y) \exp\left[\mathrm{i} \int_{x_0}^{x} \alpha(x')\, \mathrm{d}x'\right]. \tag{3}$$

Here, $\alpha(x)$ is the complex streamwise varying wave number, and $\hat{q}(x, y) = (\hat{\rho}, \hat{u}, \hat{v}, \hat{w}, \hat{T})^{\mathrm{T}}$ denotes the amplitude functions. We impose the Dirichlet boundary conditions $\tilde{u} = \tilde{v} = \tilde{w} = \tilde{T} = 0$ at the wall and force the disturbances to decay at the farfield boundary so that $\tilde{u} = \tilde{w} = \tilde{T} = \tilde{\rho} = 0$. Neumann boundary conditions are used for $\tilde{v}$ at the farfield. Linear extrapolation is used at the outlet. A sixth-order finite-difference scheme in both spatial directions is used for the discretization of PSE and HLNSE. The same computational nonuniform grids used for the basic state computations are used for the PSE and HLNSE.

We approximate the onset of transition from laminar to turbulent flow as the streamwise location where the logarithmic amplification ratio (N-factor) of any fixed-frequency disturbance reaches a critical value of N_{tr}. The mathematical expression for the N-factor is given by

$$N(x) = \frac{1}{2} \ln\left[\frac{E(x)}{E(x_{\text{lb}})}\right]. \tag{4}$$

Here, x_{lb} is the lower branch location where the disturbance first becomes unstable. The energy norm denoted by E is the following:

$$E(x) = \int_y \breve{q}(x,y)^{\mathrm{H}} \mathrm{diag}\left[\frac{\bar{T}(x,y)}{\gamma\bar{\rho}(x,y)M^2}, \bar{\rho}(x,y), \bar{\rho}(x,y), \bar{\rho}(x,y), \frac{\bar{\rho}(x,y)}{\gamma(\gamma-1)\bar{T}(x,y)M^2}\right]\breve{q}(x,y)\mathrm{d}y. \tag{5}$$

Similar to Hildebrand *et al.* [22,37], we investigate the possibility of correlating the onset of transition with the location where $N(x_{\mathrm{tr}}) = N_{\mathrm{tr}}$. We make the assumption that N_{tr} in the presence of a FFS is the same as that determined for a smooth flat plate. This assumption is reasonable so long as the onset of transition is dominated by a similar instability mechanism as the smooth plate, namely, Tollmien-Schlichting waves. For example, in the BFS flow configuration, the assumption of $N(x_{\mathrm{tr}}) = N_{\mathrm{tr}}$ being a constant led to good correlation with the experimental data by Wang and Gaster [5] until transition moved very close to the step. The local nonparallel growth rate is defined as

$$\sigma(x) = \frac{\mathrm{d}N(x)}{\mathrm{d}x} = -\alpha_i(x) + \frac{1}{2\hat{E}(x)}\frac{\mathrm{d}\hat{E}(x)}{\mathrm{d}x}, \tag{6}$$

where $\hat{E}$ refers to the energy norm of Eq. (5) calculated with $\hat{q}(x,y)$ instead of $\breve{q}(x,y)$. To perform global stability analysis based on the HLNSE, the angular frequency in Eq. (1) is replaced by a complex value $\Omega = \omega + i\sigma_t$, where σ_t is defined as the temporal growth rate of the disturbance. After setting $\breve{f} = 0$, Eq. (2) can be written as the generalized eigenvalue problem

$$A\breve{q} = \Omega B\breve{q}, \tag{7}$$

where the leading eigenvalues Ω and eigenvectors $\breve{q}$ are calculated with the Arnoldi method [43]. We apply global stability analysis to many basic states with different step heights to confirm they are uncritical. The bifurcation from globally stable flow to globally unstable flow is found and examined for one selected freestream velocity.

IV. RESULTS

In this section, we first examine the significant effects of the FFS height on the basic state, which includes the velocity components, pressure coefficient, size of the separation bubbles, and the skin-friction coefficient. After, we apply stability analysis using a combination of PSE and HLNSE to many FFS basic states with a ninety degree step angle and rounded step corners. Next, we investigate the impact that different step angles and top corner radii have on the basic state, stability analysis, and transition prediction. Finally, comparisons are made between our computational FFS results and experimental measurements by Wang and Gaster [5], along with new experimental measurements by Heintz and Scholz [18].

A. Basic states

The laminar two-dimensional basic state of $U_\infty = 34$ m/s flow over a sharp FFS at $h = 1.5$ mm with contours of nondimensional streamwise and wall-normal velocities, along with contours of the pressure coefficient, is depicted in Fig. 4. For $U_\infty = 34$ m/s or $\mathrm{Re}_s = 6.78 \times 10^5$, the boundary-layer displacement thickness is $\delta_s^* = 6.26 \times 10^{-4}$ m and $h = 1.5$ mm corresponds to $h/\delta_s^* = 2.4$. In Fig. 4, the bottom separation bubble extends from $(x - x_s)/\delta_s^* = -25$ to $(x - x_s)/\delta_s^* = 0$, while the top separation bubble extends from $(x - x_s)/\delta_s^* = 0$ to $(x - x_s)/\delta_s^* = 58$. There is a peak in the wall-normal velocity near the upper corner of the FFS. Moreover, in Fig. 4, the pressure coefficient first increases upstream of the FFS, then undergoes a sharp decrease around the upper corner of the step, after which it slowly increases downstream.

Figure 5 displays the variation of the laminar basic states via contours of nondimensional streamwise velocity for FFS heights of $h = 0.5$, 1, 1.5, and 2 mm and a fixed $U_\infty = 28$ m/s. When

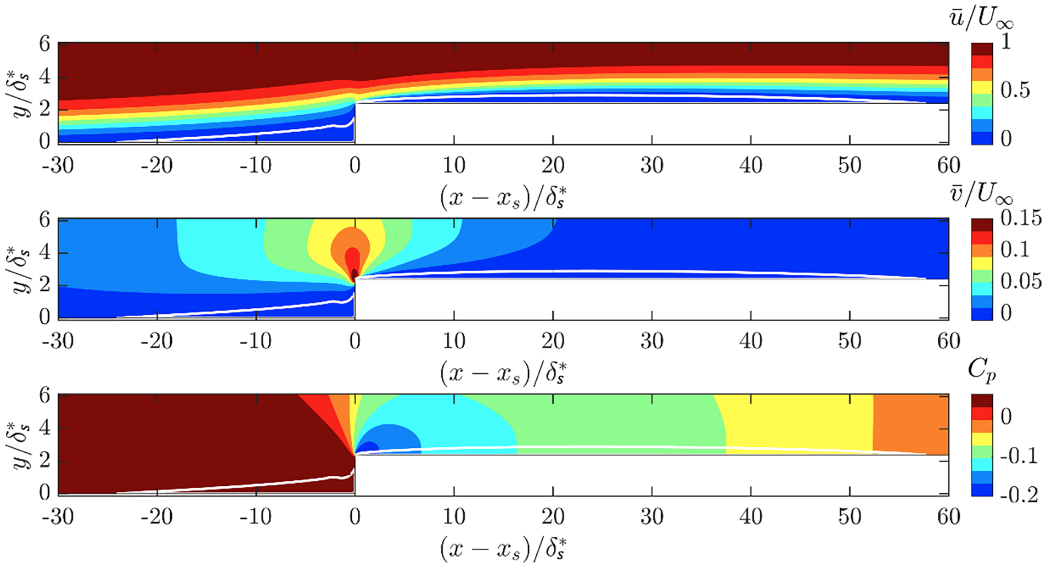

FIG. 4. Contours of the nondimensional streamwise and wall-normal velocity components, along with contours of the pressure coefficient, for subsonic flow over a FFS at $U_\infty = 34$ m/s, $\delta_s^* = 6.26 \times 10^{-4}$ m, and $h = 1.5$ mm or $\mathrm{Re}_s = 6.78 \times 10^5$ and $h/\delta_s^* = 2.4$. The separation streamlines are depicted as white lines.

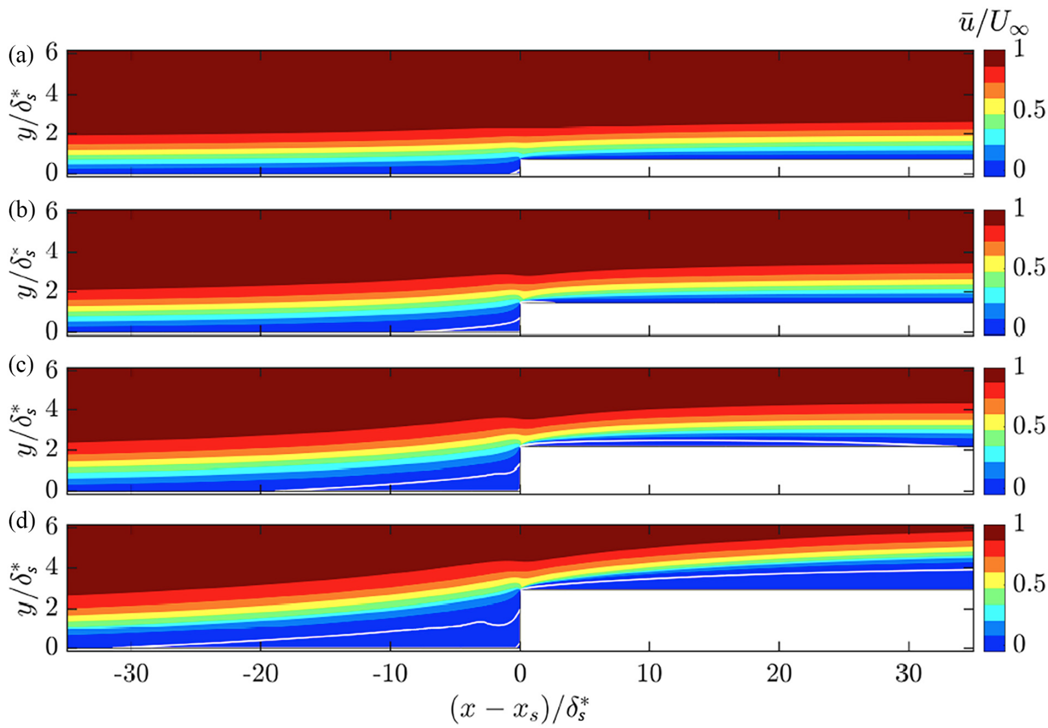

FIG. 5. Contours of nondimensional streamwise velocity contours for subsonic flow over a FFS at $U_\infty = 28$ m/s or $\mathrm{Re}_s = 5.58 \times 10^5$ with (a) $h = 0.5$ mm, (b) $h = 1$ mm, (c) $h = 1.5$ mm, and (d) $h = 2$ mm. The corresponding nondimensional values are (a) $h/\delta_s^* = 0.72$, (b) $h/\delta_s^* = 1.45$, (c) $h/\delta_s^* = 2.17$, and (d) $h/\delta_s^* = 2.90$ with $\delta_s^* = 6.9 \times 10^{-4}$ m. Moreover, the separation streamlines are depicted as white lines.

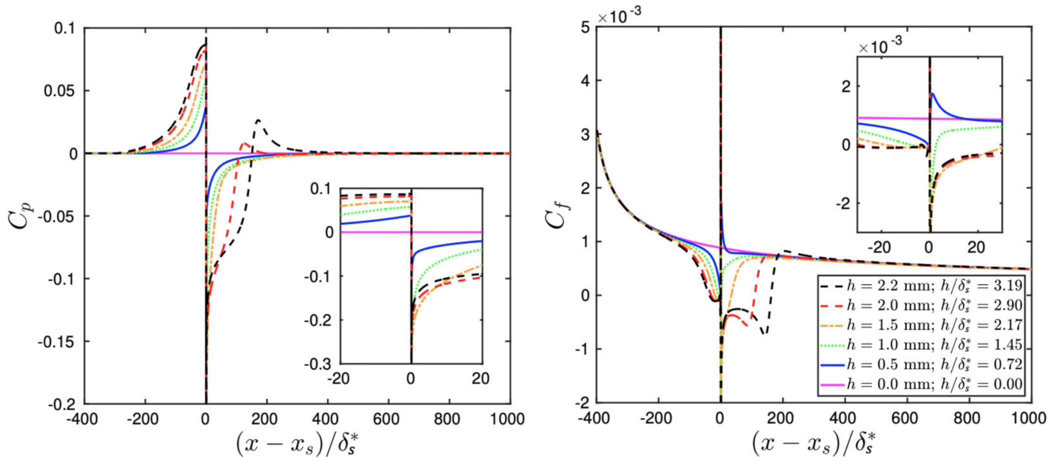

FIG. 6. Distributions of the pressure coefficient (left) and the skin-friction coefficient (right) for subsonic flow over a FFS at $U_\infty = 28$ m/s or $\mathrm{Re}_s = 5.58 \times 10^5$ with step heights ranging from $h = 0$ to 2.2 mm or $h/\delta_s^* = 0$ to 3.19.

normalized by the boundary-layer displacement thickness ($\delta_s^* = 6.9 \times 10^{-4}$ m) at the step location for $U_\infty = 28$ m/s or $\mathrm{Re}_s = 5.58 \times 10^5$ the above step heights correspond to $h/\delta_s^* = 0.725$, 1.45, 2.17, and 2.9, respectively. At $h = 0.5$ mm, the upstream separation bubble is very small in the streamwise extent, and the downstream separation bubble has not appeared yet. For $h = 1$ mm, the upstream separation bubble extends from $(x - x_s)/\delta_s^* = -8$ to 0, and the downstream separation bubble extends from $(x - x_s)/\delta_s^* = 0$ to 3. The lengths of both separation bubbles increase substantially from $h = 1$ mm to 2 mm. At the largest step height of 2 mm, the upstream separation bubble extends from $(x - x_s)/\delta_s^* = -32$ to 0, and the downstream separation bubble extends from $(x - x_s)/\delta_s^* = 0$ to 154. The separation bubble lengths at a fixed (dimensional) step height also increase at larger freestream velocities, which can been seen by comparing Figs. 4 and 5 for $h = 1.5$ mm.

We show the streamwise variation of the pressure and skin-friction coefficients along the wall at $U_\infty = 28$ m/s for FFS heights of $h = 0.5$, 1, 1.5, 2.0, and 2.2 mm in Fig. 6. The pressure coefficient increases from a value of zero to its peak value just before the step location, where it experiences a very abrupt drop, after which the pressure coefficient increases back to a value of zero. Also, the maxima and minima of the pressure coefficient become larger in magnitude with increasing step height. For the BFS results [37], the pressure coefficient decreases just before the step, experiences a strong increase at the step location, and then decreases back to zero downstream. This behavior of the pressure coefficient in the presence of a BFS is the opposite of what is experienced in the presence of a FFS with the same flow conditions and step height. For the smooth flat plate, the pressure coefficient is zero and the skin-friction coefficient varies from 0.003 to 0.0005 across $(x - x_s)/\delta_s^* = -400$ to 1000 with no separation bubble. In Fig. 6, as the FFS height increases, the regions of negative skin friction become larger. This means the separation bubbles become longer in the streamwise direction, which can also be seen in Fig. 5. There is an overshoot in the pressure coefficient around $(x - x_s)/\delta_s^* = 150$ before approaching zero downstream in Fig. 5 for $h \geqslant 2$ mm, along with a local minimum in the skin-friction coefficient. As the separation bubble on top of the FFS grows with the step height, there is a downstream shift in the location of the maximum reverse velocity between $h = 1.75$ mm and $h = 2$ mm. This shift is accompanied by the appearance of a local minimum in the skin friction and a local maximum in the pressure coefficient near reattachment. For the BFS results [37], there is no region of negative skin friction or separation that occurs before the step location only after it.

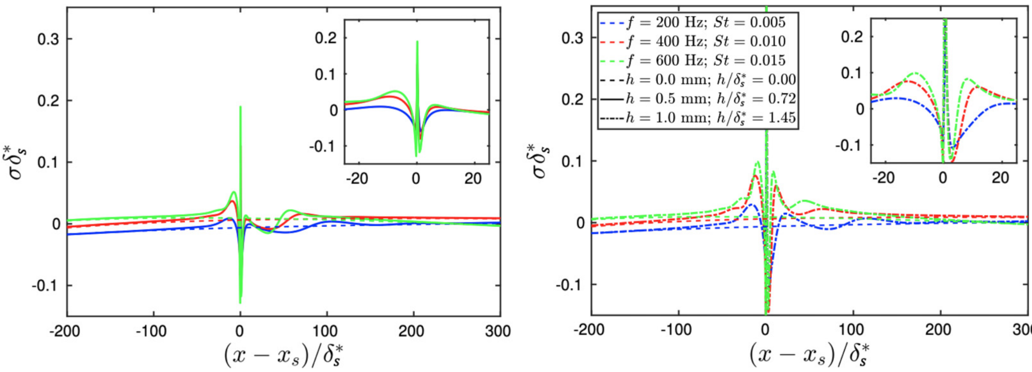

FIG. 7. Spatial growth rates of TS waves for subsonic flow over a FFS at $U_\infty = 28$ m/s or $\mathrm{Re}_s = 5.58 \times 10^5$ with three different step heights and frequencies.

B. Stability analysis

After investigating the effect of step height on the laminar basic states, we apply PSE and HLNSE about them to predict the disturbance amplification characteristics for a vertical step ($\theta = 90^\circ$) with a nominally sharp top corner of 1 μm. Figure 7 depicts the nondimensional spatial growth rates of planar TS waves for no-step and FFS cases at $U_\infty = 28$ m/s. Three representative frequencies are considered for these cases: $f = 200$ Hz, 400 Hz, and 600 Hz. In terms of the Strouhal number defined as $St = f\delta_s^*/U_\infty$, they yield $St = 0.005, 0.010$, and 0.015. The growth rates for the FFS cases agree with the smooth flat-plate case upstream of $(x - x_s)/\delta_s^* = -150$ and downstream of $(x - x_s)/\delta_s^* = 200$ in Fig. 7. Moreover, the relative changes in the growth rates near the step location become greater as the step height increases from $h = 0.5$ mm to $h = 1$ mm. Large streamwise gradients in the growth rates occur across very short distances in the vicinity of $(x - x_s)/\delta_s^* = 0$ for a FFS, which is not the case for a BFS with similar heights [22,37]. The change in TS amplification rate is slightly positive as the flow approaches the FFS, consistent with the adverse pressure gradient in this region, then it drops sharply just before the step location. After that, it quickly increases to a peak, i.e., strong destabilization as the pressure begins to increase again, then drops immediately after until finally the growth rate increases another time and eventually converges to its value over a smooth flat plate. However, for the BFS results [37], the change in TS amplification rate is slightly negative before the step location, then it sharply increases to a peak value just downstream of the step, after which it decreases and converges to its value over a smooth flat plate.

To obtain the N-factor curves and envelopes, we must integrate the spatial growth rates. Figure 8 displays the N-factor curves and envelopes for the no-step and FFS cases at $U_\infty = 28$ m/s. The same three frequencies and step heights in Fig. 7 are considered in Fig. 8. We define the N-factor envelopes by the local maximum at each streamwise station of the collective N-factor curves that correspond to a large number of individual frequencies. For both PSE and HLNSE, we ran frequencies that range from 100 Hz to 1200 Hz with increments of 20 Hz. This corresponds to a minimum and maximum Strouhal number of 0.0025 and 0.03 with increments of 0.0005 for a freestream velocity of 28 m/s. In total, 55 frequencies are considered for one FFS case with PSE and HLNSE. Upstream of the step location in Fig. 8, the N-factor curves and envelopes agree between the no-step and FFS cases. Downstream past $(x - x_s)/\delta_s^* = 3300$, the N-factor envelopes match between the no-step and FFS cases as well. This behavior is expected because the flow that is far enough upstream or downstream of the step location should not have any impact from the FFS. Lower frequencies in Fig. 8 have larger peak N-factor values. Also, the peak N-factor values grow as the step height increases from $h = 0.5$ to 1 mm. For the FFS case with $h = 0.5$ mm, the N-factor envelope is roughly parallel with the no-step envelope. However, for the FFS case with $h = 1$ mm,

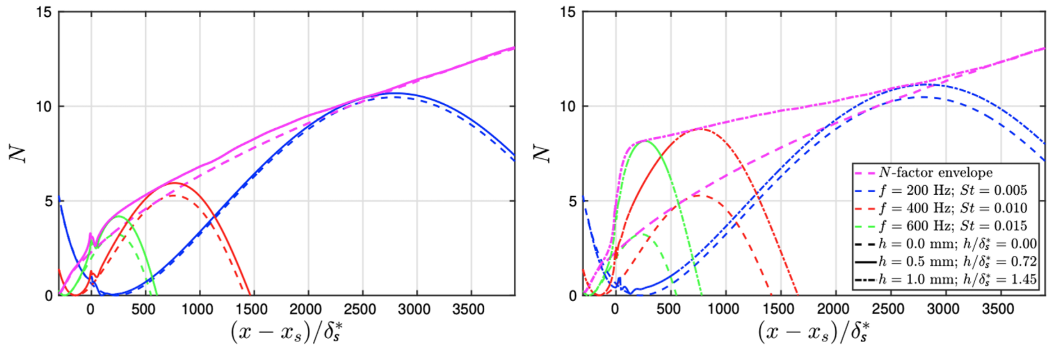

FIG. 8. N-factor curves at three selected frequencies and N-factor envelopes of TS waves for subsonic flow over a FFS at $U_\infty = 28$ m/s or $\mathrm{Re}_s = 5.58 \times 10^5$.

there is a large growth in the N-factor envelope at the step location, after which it becomes nearly flat.

Figure 9 depicts the N-factor curves that correspond to planar TS waves for a FFS step height of 1.5 mm and $U_\infty = 28$ m/s at frequencies of 200 Hz, 400 Hz, and 600 Hz from PSE and HLNSE. In terms of the nondimensional values, $\mathrm{Re}_s = 5.58 \times 10^5$, $h/\delta_s^* = 2.17$, and the Strouhal numbers are $St = 0.005, 0.010,$ and 0.015. The different N-factor curves from PSE are not plotted from $(x - x_s)/\delta_s^* = -200$ to 500 because of the upstream and downstream separation bubbles that are likely to violate the PSE assumption of a slow-varying flow in the streamwise direction. Notice there is excellent agreement between the PSE and HLNSE results in Fig. 8. This confirms that our numerical methodology of applying HLNSE in a small region around the FFS and PSE elsewhere is accurate, while also being more computationally efficient than using HLNSE everywhere. In Figs. 7–9, we plot the stability results upstream of the neutral location, which is defined as the streamwise position where the instability waves neither grow or decay. The growth rate is negative upstream of the step in Fig. 7 and increases downstream eventually crossing the neutral location or $\sigma = 0$. This negative growth rate upstream of the step causes the N-factor value to decrease until reaching a value of zero in Fig. 8. Afterward, the growth rate and N-factor value both start

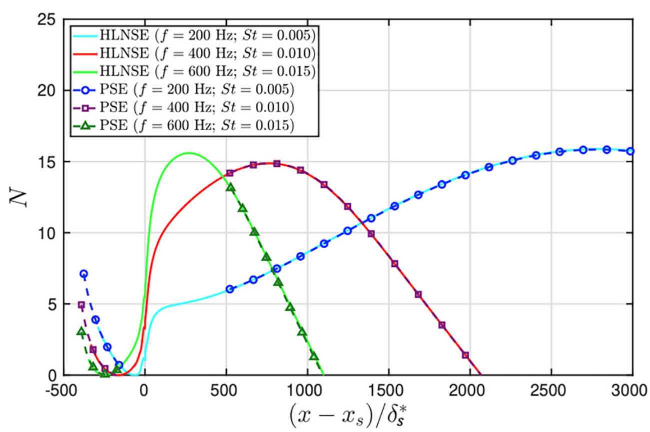

FIG. 9. Comparisons of N-factor curves at three selected frequencies between HLNSE and PSE corresponding to planar TS waves for subsonic flow over a FFS at $U_\infty = 28$ m/s or $\mathrm{Re}_s = 5.58 \times 10^5$ with a step height of 1.5 mm or $h/\delta_s^* = 2.17$ given $\delta_s^* = 6.9 \times 10^{-4}$ m.

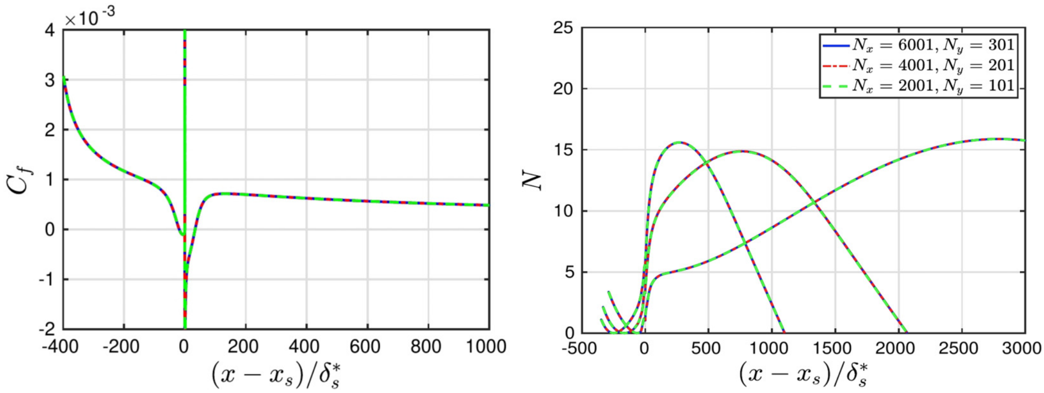

FIG. 10. Grid convergence of the skin-friction coefficient (left) and the N-factor curves at three selected frequencies (right) corresponding to subsonic flow over a FFS at $U_\infty = 28$ m/s or $\mathrm{Re}_s = 5.58 \times 10^5$ with a step height of 1.5 mm or $h/\delta_s^* = 2.17$ given $\delta_s^* = 6.9 \times 10^{-4}$ m. The selected frequencies are 200 Hz, 400 Hz, and 600 Hz or in terms of the Strouhal number are 0.005, 0.010, and 0.015.

to increase downstream. In Fig. 9, excellent agreement is obtained between results from PSE and HLNSE around the neutral location.

Figure 10 displays the grid convergence of the basic state and the stability results by showing contours of the skin-friction coefficient and the same N-factor curves that are plotted in Fig. 9 for three different resolutions. The skin-friction coefficient distributions and the N-factor curves do not change with decreasing grid resolution from $N_x = 6001$ and $N_y = 301$ to $N_x = 2001$ and $N_y = 101$ in Fig. 10. Hence, both the basic state and the stability results are grid converged. The eigenvalue mode shapes that correspond to the N-factor curves in Figs. 9 and 10 are shown in Fig. 11 near the step location. For an incompressible flat-plate configuration, the instability mode that causes transition is associated with TS waves [44]. In Fig. 11, the oscillating sign and increasing magnitude of the streamwise velocity perturbation as the flow travels downstream matches the structure of planar TS waves. We verified that oblique TS waves (i.e., nonzero spanwise wave number) do not cause significant growth for the flow conditions and FFS geometry considered in this work.

The various N-factor envelopes for the flow over a FFS at $U_\infty = 28$, 30, 32, and 34 m/s with $h = 0$, 0.25, 0.5, 0.75, 1, and 1.5 mm are displayed in Fig. 12. As the freestream velocity increases, the N-factor envelopes shift upward (i.e., the N-factor value grows). Furthermore, as the FFS height increases, the N-factor envelopes shift upward. In Fig. 12, the N-factor envelopes corresponding to $h \geqslant 1$ mm have a very large increase at the step location, after which they appear flat until converging to their respective no-step envelopes downstream. At $U_\infty = 34$ m/s, Wang and Gaster [5] measured the onset of transition at $x = 1.061$ m, which is $(x - x_s)/\delta_s^* = 1215$ in Fig. 12(d) for a smooth flat plate. This corresponds to a critical N-factor value of 7.6. Note that $N_{\mathrm{tr}} = 7.6$ is very close to 7.4, which is the value Wang and Gaster [5] used on the basis of classical parallel linear stability theory. Similar to our previous work [22,37], we use $N_{\mathrm{tr}} = 7.6$ to determine the onset of transition in every case. In Fig. 12, a change of N_{tr} by a value of one (the horizontal black dashed line) will result in a major shift of the predicted transition locations because the N-factor envelopes are very flat, i.e., $\mathrm{d}N/\mathrm{d}x$ becomes nearly 0.

We apply global stability analysis to basic states at $U_\infty = 28$ m/s or $\mathrm{Re}_s = 5.58 \times 10^5$ with step heights between $h = 2$ mm and 2.2 mm or $h/\delta_s^* = 2.9$ to 3.2. The spectra from global stability analysis shows two families of modes that become unstable for the studied cases and are identified as low- and high-wave-number modes. Figure 13 shows the variation in nondimensional frequency, temporal growth rate, and spanwise wave number of two global modes that bifurcate from stable to unstable. The global eigenvalue mode shapes are shown in Fig. 13 as well. We confirm in

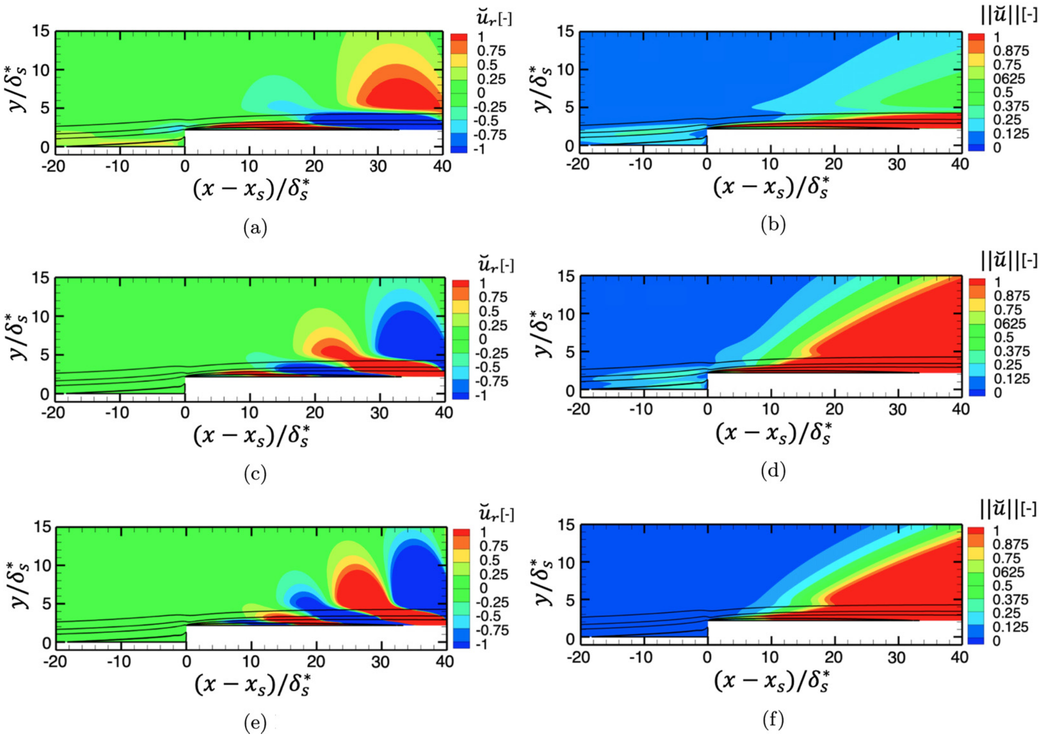

FIG. 11. Eigenvalue mode shapes from HLNSE corresponding to planar TS waves for a FFS at $U_\infty = 28$ m/s or $\mathrm{Re}_s = 5.58 \times 10^5$ with a step height of 1.5 mm or $h/\delta_s^* = 2.17$ given $\delta_s^* = 6.9 \times 10^{-4}$ m. The real part of the streamwise velocity perturbation has been normalized so its minimum and maximum values are -1 and 1, while the streamwise velocity perturbation magnitude has been normalized so its minimum and maximum values are 0 and 1. Furthermore, the black lines correspond to nondimensional streamwise velocity contours of the basic state at 0, 0.3 0.6, and 0.9. (a) Real part at $f = 200$ Hz or $St = 0.005$, (b) Magnitude at $f = 200$ Hz or $St = 0.005$, (c) Real part at $f = 400$ Hz or $St = 0.010$, (d) Magnitude at $f = 400$ Hz or $St = 0.010$, (e) Real part at $f = 600$ Hz or $St = 0.015$, and (f) Magnitude at $f = 600$ Hz or $St = 0.015$.

Fig. 13 that for $h \leqslant 2$ mm, the flow is globally stable. Once the FFS height increases to a value of 2.05 mm or $h/\delta_s^* = 2.97$, a global mode shifts from being stable to unstable. This global mode is stationary with zero frequency. It primarily resides on top of the step in the downstream separation bubble. The unstable global mode in Fig. 13(e) has a wavelength that is approximately equal in value to the downstream separation bubble length. As the FFS height continues to increase, another global mode becomes unstable at 2.15 mm or $h/\delta_s^* = 3.12$. This global mode has a varying nondimensional frequency or Strouhal number of around 0.0034 to 0.003625. It primarily resides in the upstream separation bubble with a component that exists along the shear layer downstream. The unstable global mode in Fig. 13(f) has a wavelength that is roughly equivalent to the upstream separation bubble length. Both of these distinct global modes become more unstable as the step height increases to 2.2 mm or $h/\delta_s^* = 3.2$. This analysis shows that the flow becomes globally unstable for large step heights for which the N-factor calculations predict transition at the step location.

C. Influence of step angle and top corner radius

Previous results have focused on the FFS geometry with a ninety degree slope (i.e., sharp or vertical) and top corner radius of 1 μm to closely match the Wang and Gaster [5] experimental wind

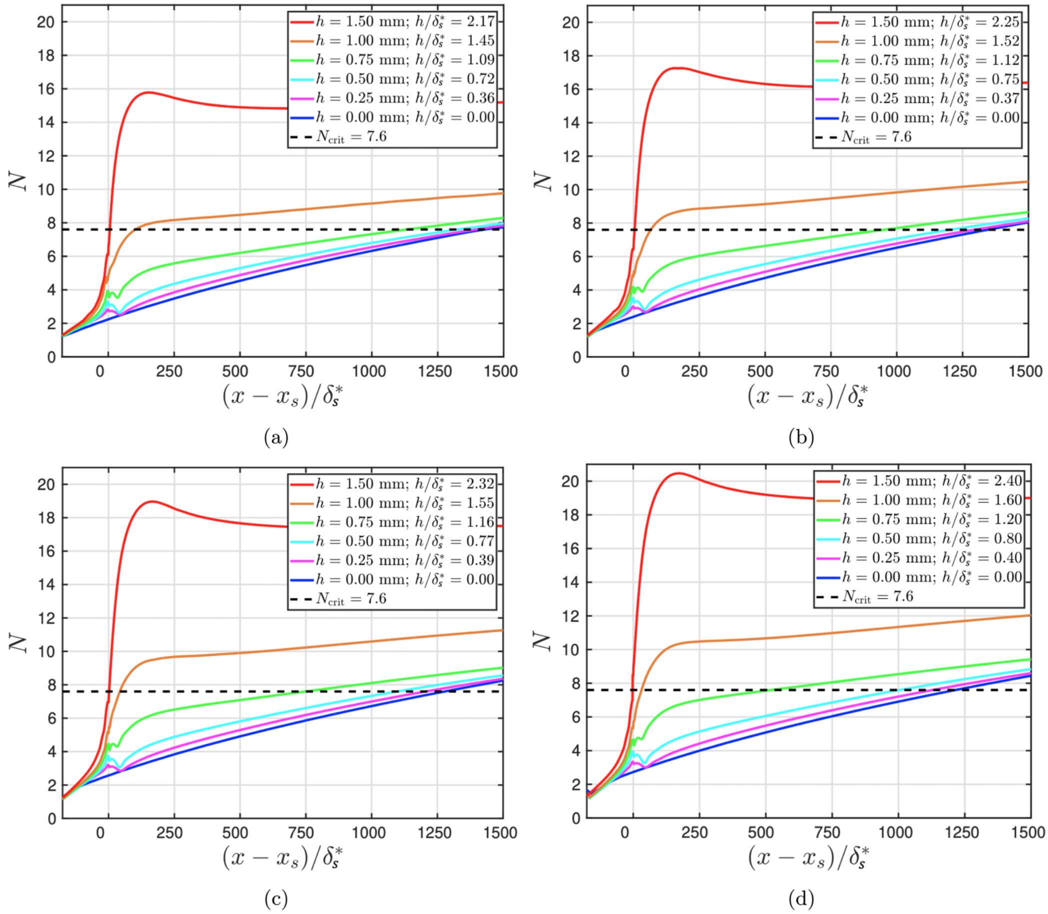

FIG. 12. N-factor envelopes corresponding to planar TS waves for a FFS at different freestream velocities and step heights. The black dashed line corresponds to a critical N-factor value of 7.6. (a) $U = 28$ m/s or $Re_s = 5.58 \times 10^5$, (b) $U = 30$ m/s or $Re_s = 6.00 \times 10^5$, (c) $U = 32$ m/s or $Re_s = 6.39 \times 10^5$, and (d) $U = 34$ m/s or $Re_s = 6.78 \times 10^5$.

tunnel configuration. We also ran simulations and performed stability analysis about FFS geometries that had varying step slope along with cases that had a larger top corner radius of 0.1 mm. A major difference between a BFS and FFS in terms of accurately predicting the onset of transition is related to the impact of the step slope. To indicate that a sharp FFS yields significantly different results than a smooth FFS, which is not the case for a BFS [37], we plot the streamwise lengths of the separation bubbles that occur both upstream and downstream of the FFS in Fig. 14, along with the maximum N-factor value at $f = 400$ Hz versus the step angle. We select a frequency of 400 Hz because it results in a maximum N-factor value close to $N_{\text{tr}} = 7.6$. The equation that defines the smooth FFS is given by

$$y_{\text{wall}}(x) = \begin{cases} 0, & \text{if } x < x_s, \\ \frac{h}{2}\left(1 + \cos\left[\pi\left(\frac{x - x_s}{x_f - x_s} + 1\right)\right]\right), & \text{if } x_s \leqslant x \leqslant x_f, \\ h, & \text{if } x > x_f, \end{cases} \tag{8}$$

where x_s and $x_f = x_s + h/\tan(\theta)$ are the start and end points of the step. Here, $\tan(\theta)$ is the maximum slope of the FFS. For this case, the flow conditions are $U_\infty = 28$ m/s, $h = 1.0$ mm, and

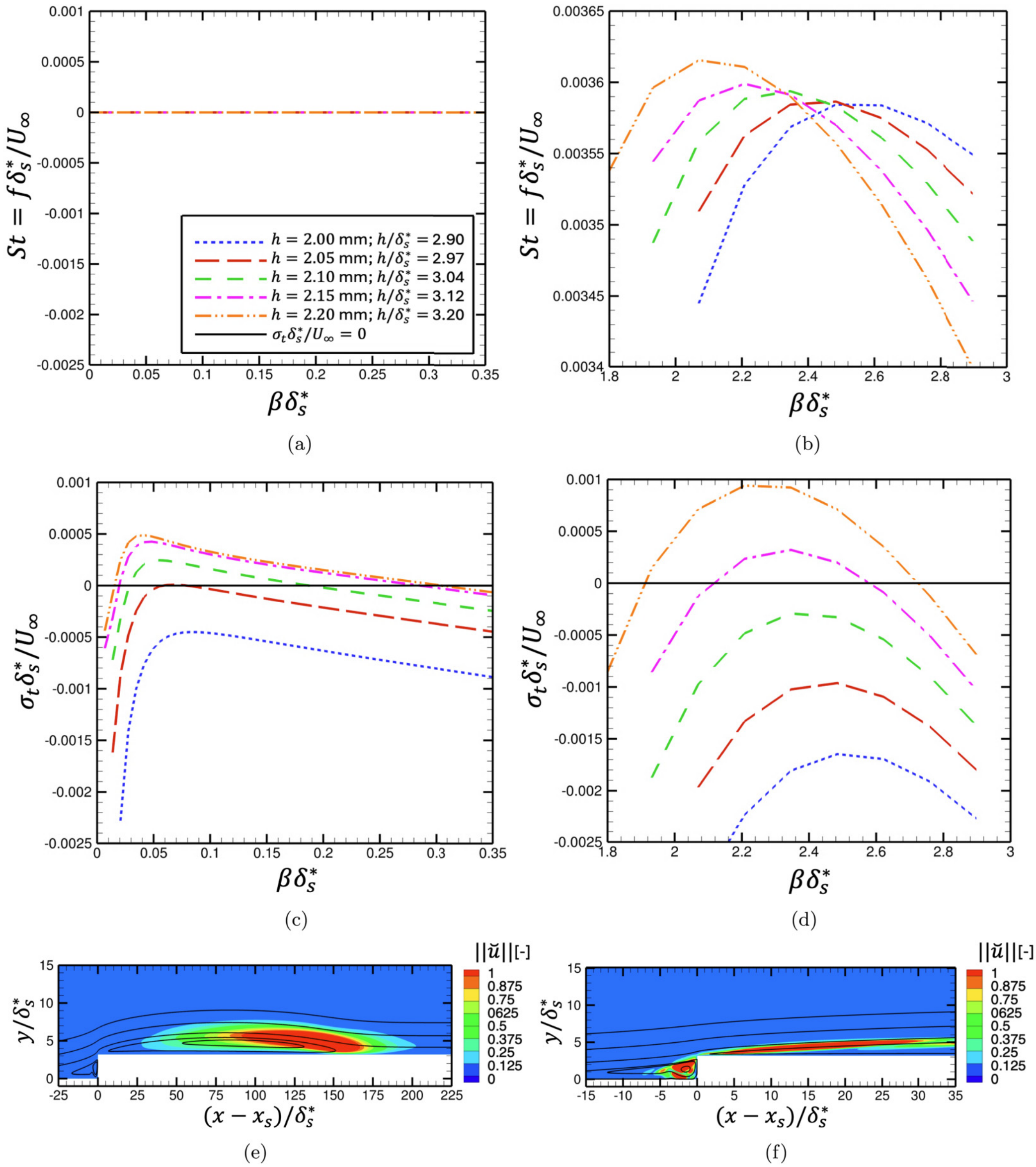

FIG. 13. Variation of the frequency, temporal growth rate, and spanwise wave number of two global modes that bifurcate from stable to unstable for subsonic flow over a FFS at $U_\infty = 28$ m/s or $\mathrm{Re}_s = 5.58 \times 10^5$. The global eigenvalue mode shapes for $h = 2.2$ mm or $h/\delta^* = 3.2$ are shown too, where the black lines are representative streamlines. Here, the stationary mode in panel (e) has $\beta\delta_s^* = 0.0345$, while the nonzero frequency mode in panel (f) has $\beta\delta_s^* = 2.208$. (a) Low-wave number frequencies, (b) High-wave number frequencies, (c) Low-wave number growth rates, (d) High-wave number growth rates, (e) Low-wave number global mode shape (not to scale), and (f) High-wave number global mode shape.

$\delta_s^* = 6.9 \times 10^{-4}$ m. The corresponding nondimensional values are $\mathrm{Re}_s = 5.58 \times 10^5$, $h/\delta_s^* = 1.45$, and $\mathrm{St} = 0.01$.

In Fig. 14(a), the upstream separation bubble is present for $\theta \geqslant 10^\circ$, and the downstream separation bubble is present for $\theta \geqslant 75^\circ$. As the step angle increases from 10° to 90°, the separation length

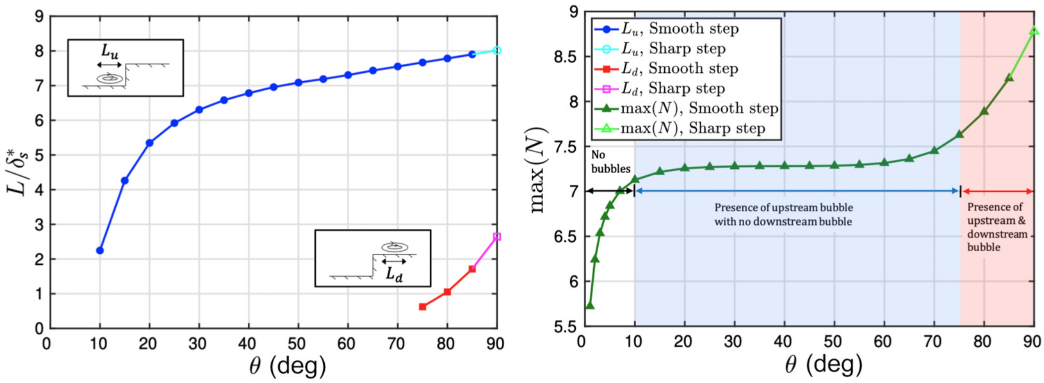

FIG. 14. Lengths of the separation bubbles that occur upstream (L_u) and downstream (L_d) of the smooth/sharp FFS versus the step angle (left) and the maximum N-factor value at $f = 400$ Hz or St $= 0.01$ versus the step angle (right) at $U_\infty = 28$ m/s, $\delta_s^* = 6.9 \times 10^{-4}$ m, and $h = 1.0$ mm. The corresponding nondimensional values are $\mathrm{Re}_s = 5.58 \times 10^5$ and $h/\delta_s^* = 1.45$.

of the upstream bubble progressively gets larger and never levels out. Similarly, the separation length of the downstream bubble increases with the step angle. Notice that in Fig. 14(b), the maximum N-factor value sharply increases from $\theta = 1^\circ$ to $\theta = 10^\circ$. Following the upstream bubble formation at $\theta = 10^\circ$, the N-factor value starts to level out until slightly before the formation of a second bubble just downstream of the step when $\theta = 75^\circ$, at which point the N-factor value increases sharply again to its limiting value at $\theta = 90^\circ$. In recent experiments by Eppink and Casper [45] in the two-foot-by-three-foot low-speed boundary-layer channel at the NASA Langley Research Center, a downstream separation bubble on top of the FFS was not present for step angles of $\theta = 30^\circ$ and $\theta = 45^\circ$, which agrees with our computational mean flow results. For the BFS results [37], there is just one separation bubble that occurs after the step whose length becomes larger with step slope and eventually plateaus for $\theta \geqslant 75^\circ$. The maximum N-factor value also plateaus in value for the BFS even at larger step angles, which is not the case for a FFS.

Figure 15 shows the computational grids that have two different FFS top corner radii, along with the distributions of the skin-friction coefficient for each case at $U_\infty = 28$ m/s and $h = 1.5$ mm. We already know from the results of Fig. 14 that geometry changes of the FFS can have a significant effect on the laminar basic states and stability characteristics. In Fig. 15, the solution that corresponds to $r = 0.1$ mm has a much smaller recirculation bubble after the FFS than for the case with $r = 0.001$ mm. For $r = 0.1$ mm and $r = 0.001$ mm, the recirculation bubble lengths after the step are $L_d = 13$ and $L_d = 34$, respectively. As we will see in the following discussions and figures, the $r = 0.1$ mm solutions that have a smaller recirculation bubble after the step results in transition locations that are more downstream and in better agreement with the experimental measurements by Wang and Gaster [5], then solutions with $r = 0.001$ mm. This agrees with Fig. 14, which shows a basic state with a smaller recirculation bubble after the FFS produces N-factor values that are smaller, and hence, transition would occur further downstream. Also, this signifies that experimental measurements of the separation bubble lengths before and after the FFS would be critical for better validation with simulations and stability analysis.

D. Comparisons to experiments

After examining the results from simulations and stability analysis of flow over a flat plate with a FFS and contrasting them with a BFS, we compare those computational FFS results to experimental measurements. Figure 16 compares the experimental transition locations measured by Wang and

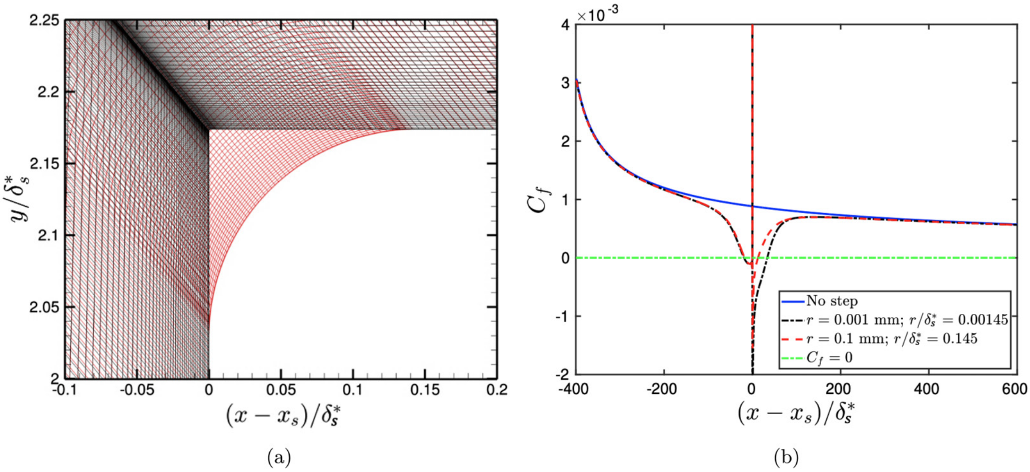

FIG. 15. The baseline grid (black, see also Fig. 2) near the FFS that has a top corner radius of 0.001 mm or $r/\delta_s^* = 0.00145$, and the rounded FFS grid (red) that has a top corner radius of 0.1 mm or $r/\delta_s^* = 0.145$, along with the skin-friction coefficient for each case at $U_\infty = 28$ m/s, $\delta_s^* = 6.9 \times 10^{-4}$ m, and $h = 1.5$ mm. The corresponding nondimensional values are $\mathrm{Re}_s = 5.58 \times 10^5$ and $h/\delta_s^* = 2.17$. (a) Computational grid and (b) Skin-friction coefficient.

Gaster [5] to our computational predictions with freestream velocities ranging from 16 to 34 m/s and FFS heights from 0 to 2 mm. We include solutions with two different FFS top corner radii of 0.001 and 0.1 mm. For the smooth flat-plate cases, there is excellent agreement between the computational and experimental transition locations. However, there is not as good of agreement between the experimental and computational transition locations for nonzero FFS heights. The larger top corner radius of 0.1 mm leads to somewhat reduced discrepancy between the computational predictions and the measured data when compared to a smaller top corner radius of 0.001 mm. For the nonzero FFS heights, the computational predictions are significantly upstream of the measured transition locations. All of the predicted transition locations for $h \geqslant 1.5$ mm are very close to the step

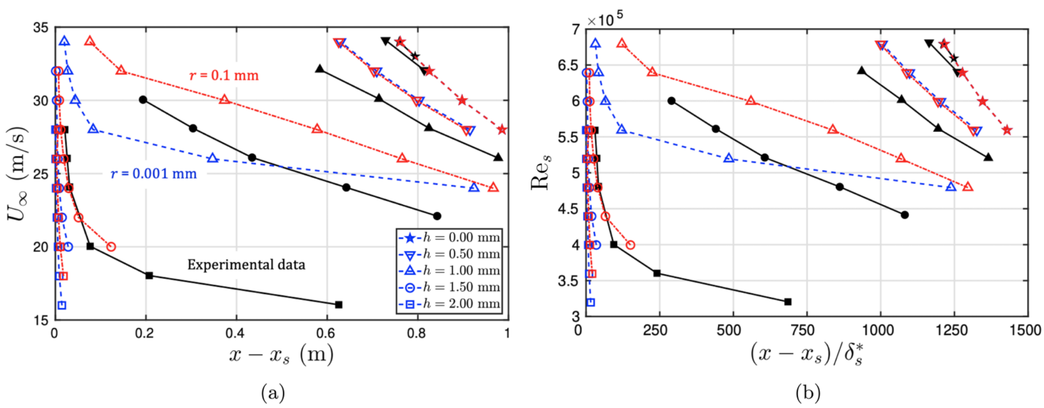

FIG. 16. Comparisons of transition locations based on $N_{\mathrm{tr}} = 7.6$ (open symbols and dashed lines) with two different top step corner radii, namely, 0.001 mm (blue) and 0.1 mm (red) to measured transition locations by Wang and Gaster [5] (close symbols and solid black lines) for subsonic flow over a FFS. (a) Dimensional units and (b) Nondimensional units.

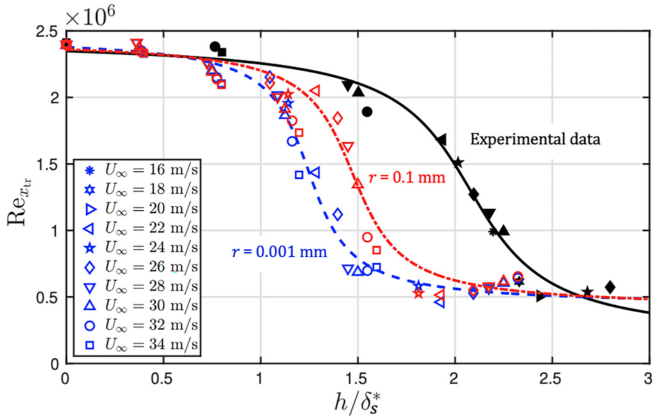

FIG. 17. Variation of the Reynolds number based on the location of transition onset versus step height. The filled black symbols are experimental data [5], and the open symbols are computational predictions with top step corner radii of 0.001 mm (blue) and 0.1 mm (red). Furthermore, the solid and dashed lines denote curve fits of the experimental and numerical data, respectively.

location. Even for the smallest FFS height of 0.5 mm, there is considerable disagreement between the simulations and experiments. The overall disagreement between the simulations and experiments is likely due to strong gradients in the pressure (Fig. 6) and the growth rates (Fig. 7) across really small distances at the FFS location, which causes the N-factor envelopes to rise sharply and then plateau (Fig. 12). This causes the N-factor method to become highly sensitive to small variations in the critical or transition N-factor value, N_{tr}. We still capture the overall trend from the experiments with our computational predictions, which is that as the FFS height and freestream velocity increase, the onset of transition shifts upstream toward the step location.

We show comparisons of the measured and prediction transition locations in terms of the Reynolds number based on the location of transition onset, $\mathrm{Re}_{x_{\mathrm{tr}}} = \rho_\infty U_\infty x_{\mathrm{tr}}/\mu_\infty$, versus the FFS height scaled by the displacement thickness of the boundary layer at the step location, h/δ_s^*, in Fig. 17. The same freestream velocities and step heights considered in Fig. 16 are plotted in Fig. 17. Least squares fits that have the form $\mathrm{Re}_{x_{\mathrm{tr}}} = c_1 \arctan[(h/\delta_s^* - c_2)/c_3] + c_4$ of the experimental and computational data are included as part of Fig. 17. The expression $\mathrm{Re}_{x_{\mathrm{tr}}} = -0.73 \arctan[(h/\delta_s^* - 2.08)/0.295] + 1.3$ is associated with the experimental measurements (black), the expression $\mathrm{Re}_{x_{\mathrm{tr}}} = -0.647 \arctan[(h/\delta_s^* - 1.25)/0.158] + 1.44$ corresponds to simulations that have a FFS top corner radius of 0.001 mm (blue), and $\mathrm{Re}_{x_{\mathrm{tr}}} = -0.647 \arctan[(h/\delta_s^* - 1.47)/0.183] + 1.37$ corresponds to simulations that have a FFS top corner radius of 0.1 mm (red). In Fig. 17, the experimental and computational results have the exact same overall trend, except the experimental results are shifted rightward to larger values of h/δ_s^* for the same $\mathrm{Re}_{x_{\mathrm{tr}}}$ as the computational results. This amounts to only changing the constant c_2 in the above expressions (i.e., $c_2 = 1.25$ or 1.47 to 2.08) to obtain good agreement between the experimental and computational results. Comparisons between the simulation results with a FFS top corner radius of 0.1 mm and experiments yield better agreement than results with a FFS top corner radius of 1 μm, but the critical h/δ_s^* for the upstream shift of the transition location, which is correlated with c_2, is notably higher for the experimental data.

Figure 18 shows comparisons of ΔN versus h/δ_s^* between experiments and simulations for the same freestream velocities and step heights considered in Figs. 16 and 17, where ΔN is defined as the difference between smooth surface N-factors at the prediction transition locations for the no-step case and a given FFS configuration. The linear fit $\Delta N = 1.6 h/\delta_s^*$ by Crouch *et al.* [6] is depicted in Fig. 18. We also include experimental measurements by Wang and Gaster [5] in Fig. 18. Three least squares fits with the form $\mathrm{Re}_{x_{\mathrm{tr}}} = c_1 \arctan[(h/\delta_s^* - c_2)/c_3] + c_4$ are plotted in Fig. 18 with the

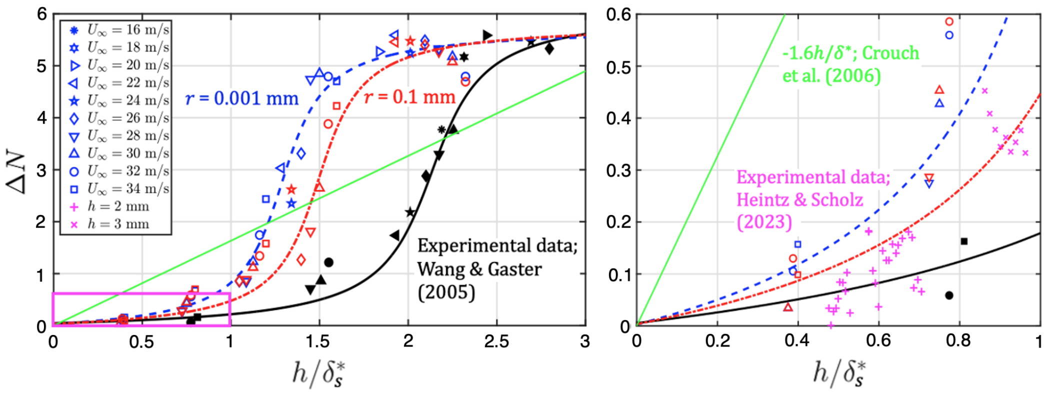

FIG. 18. Reduction in the N-factor value for transition versus step height. The filled black symbols are experimental data from Wang and Gaster [5], the open symbols are computational predictions from two different top step corner radii, and the pluses/crosses are experimental data from Heintz and Scholz [18]. Several curve fits of the experimental and computational data are shown.

experimental and computational results. The expression $\Delta N = 1.99\arctan[(h/\delta_s^* - 2.14)/0.215] - 2.93$ is associated with the experimental measurements (black) of Wang and Gaster [5], the expression $\Delta N = 1.89\arctan[(h/\delta_s^* - 1.29)/0.179] - 2.73$ corresponds to simulations that have a FFS top corner radius of 0.001 mm (blue), and $\Delta N = 1.92\arctan[(h/\delta_s^* - 1.49)/0.182] - 2.78$ corresponds to simulations that have a FFS top corner radius of 0.1 mm (red). Results in Fig. 18 indicate a highly nonlinear "S" shaped trend in both the measurements by Wang and Gaster [5] as well as the computational predictions, which is very different from the linear correlation proposed by Crouch *et al.* [6]. However, the latter appears to pass approximately through the middle of the experimental and computational data.

A zoomed-in view of ΔN versus h/δ_s^* is displayed in Fig. 18 on the right, along with the inclusion of very recent experimental measurements from Heintz and Scholz [18]. Notice that in Fig. 18, similar to Fig. 17, the experimental and computational results have the exact same overall trend, except the experimental results are shifted rightward to larger values of h/δ_s^* for the same ΔN as the computational results. Again, this amounts to only changing the constant c_2 in the above expressions (i.e., $c_2 = 1.29$ or 1.49 to 2.14) to obtain a closer agreement between the experimental and computational results. The agreement between recent experimental measurements by Heintz and Scholz [18] and our computational transition predictions in Fig. 18 is fairly good for small h/δ_s^*. Hence, additional transition experiments are needed to understand potential sources for the discrepancies with the Wang and Gaster [5] experiments and to quantify the relevant parameters to predict transition for boundary-layer flow over forward-facing steps. One of the most important parameters that we need for validation is experimental measurements of the separation bubble lengths before and after the step because they have a strong impact on the stability results and transition to turbulence (refer back to Figs. 14–16 and 18). From the results in Figs. 15 and 16, we know conclusively that a shorter length of the separation bubble on top of the FFS shifts the predicted transition locations from the simulations further downstream in better agreement with the experimental measurements of Wang and Gaster [5]. Moreover, in Fig. 14 we know that a shorter length of the upstream separation bubble results in lower N-factor values, which leads to better agreement between simulations and experiments because the predicted transition locations will be further downstream. By comparing Fig. 14 with Fig. 5 in Hildebrand *et al.* [37], we also know the stability results are way more sensitive to subtle changes in the FFS configuration than in the BFS configuration. Other factors that could influence both the separation bubble sizes and the predicted transition locations in the FFS configuration are freestream turbulence, a nonzero pressure gradient, and surface roughness.

V. CONCLUSIONS

We performed simulations and stability analysis about steady two-dimensional base flows that correspond to a nearly incompressible flat-plate boundary layer over a forward-facing step. The flow configuration was selected to match the wind tunnel experiments of Wang and Gaster [5] with freestream velocities of 16 to 34 m/s, a fixed step location of 0.3 m downstream of the plate leading edge, and step heights of 0 to 2 mm ($0 < h/\delta_s^* < 3.2$). For a majority of the flow conditions of interest, the flow in the vicinity of the FFS included two regions of flow reversal, one upstream of the FFS and the other just downstream, i.e., along the top surface. As expected, the streamwise lengths of both separation bubbles increased monotonically as the freestream velocity and/or the step height were increased. There were large streamwise gradients in the pressure and skin-friction distributions across very short distances at the FFS location of the basic states. Also, the growth rates of the TS waves computed with a combination of PSE and HLNSE had similar large gradients near the FFS location. In the case of a BFS [37], there was only a single region of flow reversal downstream of the step, and the pressure coefficient and TS growth rates were less complex near the step, i.e., less sign changes and weaker streamwise gradients, compared to a FFS case with the same conditions.

Many of the N-factor envelopes that resulted from the integration of TS growth rate curves sharply rose at the FFS location and then plateaued for long distances. This means the N-factor envelope in the downstream region is flat such that $dN/dx \approx 0$, and the N-factor method is extremely sensitive to $N_{\rm tr}$. However, this does not occur for a BFS, where the N-factor envelope is just shifted upward from the unperturbed case (some exceptions for large step heights). Furthermore, the simulation and stability results are very sensitive to changes in the FFS geometry, including the step angle and top corner radius, which is not necessarily the case for a BFS (especially for $\theta \geqslant 75^\circ$). We performed global stability analysis for the FFS configuration, and two unstable modes were found. One stationary global mode became unstable for $h/\delta^* \geqslant 2.97$ and resided in the downstream separation bubble. The other nonzero frequency global mode became unstable for $h/\delta^* \geqslant 3.12$ and resided in the upstream separation bubble.

The transition prediction based on the N-factor method for the experimental conditions and step heights with a nominally sharp and rounded steps show the same trend captured in the experimental measurements, but the predicted shift in transition location begins at smaller step height to boundary-layer thickness ratios in comparison with the experiments. Specifically, the curve fits of the form $\mathrm{Re}_{x_{\rm tr}} = c_1 \arctan[(h/\delta_s^* - c_2)/c_3] + c_4$ and $\Delta N = c_1 \arctan[(h/\delta_s^* - c_2)/c_3] + c_4$ successfully aligned with both experimental and computational data, and the constants c_1, c_3, and c_4 matched well between the measured data from Ref. [5] and the numerical predictions. However, the remaining constant c_2, which correlates with the critical h/δ_s^* for the upstream shift in transition location, showed significant disagreement between the experiments by Wang and Gaster ($c_2 = 2.14$) and the numerical computations reported here ($c_2 = 1.29$). Comparisons between our transition predictions and the recent experimental measurements by Heintz and Scholz [18] resulted in good agreement for the available data with $h/\delta_s^* < 1$. This highlights the need for more detailed transition experiments on subsonic boundary-layer flow over FFS and other roughness elements. As the FFS became smoother, either via rounding the corners or decreasing the step slope, the streamwise length of the separation bubble after the step became smaller, which in turn leads to a downstream shift of the predicted transition location along with increased c_2 values and, therefore, a closer agreement with the experimental measurements of Wang and Gaster. Hence, experimental measurements of the separation bubble lengths before and after the FFS would be critical for more validation with simulations and stability analysis.

ACKNOWLEDGMENTS

The computations described in this paper were carried out in support of the Revolutionary Computational AeroSciences discipline under the Transformational Tools and Technologies project of the NASA Transformative Aeronautics Concepts Program. The authors greatly appreciate computational resources from both the NASA Langley Research Center's K Midrange Cluster and the NASA High-End Computing Program through the NASA Advanced Supercomputing Division at the NASA Ames Research Center.

[1] F. Collier, Subsonic fixed wing project overview, NASA FAP Annual Meeting, October 2008.

[2] P. Argüelles, J. Lumsden, M. Bischoff, D. Ranque, P. Busquin, S. Rasmussen, B. A. C. Droste, P. Reutlinger, R. Evans, R. Robins, W. Kröll, H. Terho, J.-L. Lagardére, A. Wittlöv, and A. Lina, European aeronautics: A vision for 2020, Europan Commission Rept. KI-34-01-827-EN-C, January 2001.

[3] G. Schrauf, Status and perspectives of laminar flow, Aeronaut. J. **109**, 639 (2005).

[4] W. S. Saric, D. E. West, M. W. Tufts, and H. L. Reed, Experiments on discrete roughness element technology for swept-wing laminar flow control, AIAA J. **57**, 641 (2019).

[5] Y. Wang and M. Gaster, Effect of surface steps on boundary layer transition, Exp. Fluids **39**, 679 (2005).

[6] J. D. Crouch, V. S. Kosorygin, and L. L. Ng, Modeling the effects of steps on boundary-layer transition, in *IUTAM Symposium on Laminar-Turbulent Transition*, edited by R. Govindarajan (Springer, Dordrecht, Netherlands, 2006), pp. 37–44.

[7] J. Slotnick, A. Khodadoust, J. Alonso, D. Darmofal, W. Gropp, D. Mavriplis, and E. Lurie, CFD vision 2030 study: A path to revolutionary computational aerosciences, NASA/CR-2014-218178, 2014, https://ntrs.nasa.gov/citations/20140003093.

[8] D. Barkley, M. G. M. Gomez, and R. D. Henderson, Three-dimensional instability in flow over a backward-facing step, J. Fluid Mech. **473**, 167 (2002).

[9] J.-C. Loiseau, J.-C. Robinet, S. Cherubini, and E. Leriche, Investigation of the roughness-induced transition: global stability analyses and direct numerical simulations, J. Fluid Mech. **760**, 175 (2014).

[10] P. Klebanoff and K. Tidstrom, Mechanism by which a two-dimensional roughness element induces boundary layer transition, Phys. Fluids **15**, 1173 (1972).

[11] M. E. Goldstein, Scattering of acoustic waves into Tollmien-Schlichting waves by small streamwise variations, J. Fluid Mech. **154**, 509 (1985).

[12] M. M. Choudhari, Boundary-layer receptivity to three-dimensional unsteady vortical disturbances in free stream, in *Proceedings of the 34th Aerospace Sciences Meeting and Exhibit* (AIAA, Reston, VA, 1996), AIAA Paper 96-0181.

[13] M. Asai, M. Minagawa, and M. Nishioka, The instability and breakdown of a near-wall low-speed streak, J. Fluid Mech. **455**, 289 (2002).

[14] M. M. Choudhari and C. Streett, Theoretical prediction of boundary-layer receptivity, in *Proceedings of the 25th AIAA Fluid Dynamics Conference* (AIAA, Reston, VA, 1994), AIAA Paper 94-2223.

[15] B. Holmes, C. Obara, G. Martin, and C. Domack, Manufacturing tolerances for natural laminar flow airframe surfaces, SAE Paper No. 850863, 1985.

[16] A. V. Boiko, A. V. Dovgal, V. V. Kozlov, and V. A. Shcherbakov, Flow instability in the laminar boundary layer separation zone created by a small roughness element, Fluid Dyn. **25**, 12 (1990).

[17] A. V. Dovgal and V. V. Kozlov, Hydrodynamic instability and receptivity of small scale separation regions, in *Laminar-Turbulent Transition*, edited by D. Arnal and R. Michel (Springer, Heidelberg, Berlin, 1990), pp. 523–531.

[18] A. Heintz and P. Scholz, Measurements on the effect of steps on the transition of laminar boundary layers, Exp. Fluids **64**, 76 (2023).

[19] S. Ragab, A. Nayfeh, and R. C. Krishna, Stability of compressible boundary layers over a smooth backward-facing step, in *Proceedings of the 21st Fluid Dynamics, Plasma Dynamics, and Lasers Conference* (AIAA, Reston, VA, 1990), AIAA Paper 1990-1449.

[20] J. Perraud and A. Seraudie, Effects of steps and gaps on 2d and 3d transition, *European Congress on Computational Methods in Applied Science and Engineering, The International Center for Numerical Methods in Engineering* (Barcelona, Spain, 2000), pp. 1–18.

[21] C. A. Edelmann and U. Rist, Impact of forward-facing steps on laminar-turbulent transition in transonic flows, AIAA J. **53**, 2504 (2015).

[22] N. Hildebrand, M. M. Choudhari, and P. Paredes, Predicting boundary-layer transition over backward-facing steps via linear stability analysis, AIAA J. **58**, 3728 (2020).

[23] M. W. Tufts, H. L. Reed, B. K. Crawford, G. T. Duncan, and W. S. Saric, Computational investigation of step excrescence sensitivity in a swept-wing boundary layer, J. Aircr. **54**, 602 (2017).

[24] J. L. Eppink, R. W. Wlezien, R. A. King, and M. M. Choudhari, Influence of a backward-facing step on swept-wing boundary-layer transition, AIAA J. **57**, 267 (2019).

[25] A. F. Rius-Vidales and M. Kotsonis, Impact of a forward-facing step on the development of crossflow instability, J. Fluid Mech. **924**, A34 (2021).

[26] A. F. Rius-Vidales and M. Kotsonis, Unsteady interaction of crossflow instability with a forward-facing step, J. Fluid Mech. **939**, A19 (2022).

[27] J. D. Crouch, Modeling transition physics for laminar flow control, in *Proceedings of the 38th Fluid Dynamics Conference and Exhibit* (AIAA, Reston, VA, 2008), AIAA Paper 2008-3832.

[28] M. Costantini, S. Risius, C. Klein, and W. Kühn, Effect of forward-facing steps on boundary layer transition at a subsonic Mach number, *New Results in Numerical and Experimental Fluid Mechanics X*, edited by A. Dillmann, G. Heller, E. Krämer, C. Wagner, and C. Breitsamter (Springer, Cham, 2014), pp. 203–213.

[29] J. D. Crouch and V. S. Kosorygin, Surface step effects on boundary-layer transition dominated by tollmien-schlichting instability, AIAA J. **58**, 2943 (2020).

[30] J. A. Masad and M. R. Malik, Link between flow separation and transition onset, AIAA J. **33**, 882 (1995).

[31] A. Wörner, U. Rist, and S. Wagner, Humps/steps influence on stability characteristics of two-dimensional laminar boundary layer, AIAA J. **41**, 192 (2003).

[32] D. J. Wise, V. Nguyen, K. T. E. Chua, Q. V. Nguyen, T. Nadesan, and Y. Cui, DNS investigation of laminar-to-turbulent transition with favorable pressure gradient: Effects of surface imperfections, *AIAA SciTech 2020 Forum* (AIAA, Reston, VA, 2020), AIAA Paper 2020-1581.

[33] D. P. Rizzetta and M. R. Visbal, Numerical simulation of excrescence generated transition, AIAA J. **52**, 385 (2014).

[34] M. Dong and A. Zhang, Scattering of Tollmien-Schlichting waves as they pass over Forward-/Backward-Facing steps, Appl. Mathem. Mech. **39**, 1411 (2018).

[35] C. Thomas, S. M. Mughal, H. Roland, R. Ashworth, and A. Martinez-Cava, Effect of small surface deformations on the stability of Tollmien-Schlichting disturbances, AIAA J. **56**, 2157 (2018).

[36] J. A. Franco, S. Hein, and E. Valero, On the influence of two-dimensional hump roughness on laminar-turbulent transition, Phys. Fluids **32**, 034102 (2020).

[37] N. Hildebrand, P. V. Mysore, M. M. Choudhari, B. S. Venkatachari, and P. Paredes, Transition prediction of boundary layers in the presence of backward-facing steps, AIAA J. **60**, 4149 (2022).

[38] P. R. Amestoy, I. S. Duff, J. Koster, and J.-Y. L'Excellent, A fully asynchronous multifrontal solver using distributed dynamic scheduling, SIAM J. Matrix Anal. Appl. **23**, 15 (2001).

[39] C. Streett, Direct harmonic linear Navier-Stokes methods for efficient simulation of wave packets, in *Proceedings of the 36th AIAA Aerospace Sciences Meeting and Exhibit* (AIAA, Reston, VA, 1998), AIAA Paper 98-0784.

[40] P. Paredes, M. M. Choudhari, F. Li, J. Jewell, R. Kimmel, E. Marineau, and G. Grossir, Nosetip bluntness effects on transition at hypersonic speeds: Experimental and numerical analysis, J. Spacecr. Rockets **56**, 369 (2019).

[41] A. P. Haas, O. M. F. Browne, H. F. Fasel, and C. Brehm, A time-spectral approximate jacobian based linearized compressible navier-stokes solver for high-speed boundary-layer receptivity and stability, J. Comput. Phys. **405**, 108978 (2020).

[42] T. Herbert, Parabolized stability equations, Annu. Rev. Fluid Mech. **29**, 245 (1997).

[43] Y. Saad, Variations of arnoldi's method for computing eigenelements of large unsymmetric matrices, Linear Algebra Appl. **34**, 269 (1980).

[44] P. J. Schmid and D. S. Henningson, *Stability and Transition in Shear Flows*, Applied Mathematical Sciences Vol. 142 (Springer, 2012).

[45] J. L. Eppink and C. Casper, Effects of forward-facing step shape on stationary crossflow instability growth and breakdown, *AIAA Aviation 2019 Forum* (AIAA, Reston, Va, 2019), AIAA Paper 2019-3532.